We are IntechOpen, the world's leading publisher of Open Access books Built by scientists, for scientists

4,800
Open access books available

122,000
International authors and editors

135M
Downloads

Our authors are among the

154
Countries delivered to

TOP 1%
most cited scientists

12.2%
Contributors from top 500 universities

WEB OF SCIENCE™

Selection of our books indexed in the Book Citation Index in Web of Science™ Core Collection (BKCI)

Interested in publishing with us?
Contact book.department@intechopen.com

Numbers displayed above are based on latest data collected.
For more information visit www.intechopen.com

29

Frequency-Dependent Monte Carlo Simulations of Phonon Transport in Nanostructures

Qing Hao and Gang Chen
Massachusetts Institute of Technology
USA

1. Introduction

It is now widely recognized that phonon transport in micro/nanostructures is strongly affected by interfaces and boundaries, which can lead to a significantly reduced thermal conductivity (Cahill et al., 2003; Chen, 2005; McConnell & Goodson, 2005). On one hand, the reduced thermal conductivity can significantly impede heat spreading in microelectronic and photonic devices, creating challenges to thermal management (Garimella et al., 2008). On the other hand, such size effects have been exploited to develop nanostructured bulk materials with better thermoelectric (TE) performance (Hsu et al., 2004; Poudel et al., 2008; Ma et al., 2008; Wang et al., 2008; Joshi et al., 2008; Yang et al., 2009; Zhu et al., 2009). The effectiveness of a TE material is ultimately determined by its dimensionless figure of merit (ZT), defined as $ZT = S^2\sigma T / k$, where S, σ, k, T represent Seebeck coefficient, electrical conductivity, thermal conductivity, and absolute temperature, respectively (Goldsmid, 1964). In nanostructured bulk materials, nanostructured interfaces can be designed to strongly scatter phonons but only slightly affect the charge carrier transport. This approach leads to a significant reduction in the lattice thermal conductivity k_L, and in some cases a simultaneous increase of the power factor $S^2\sigma$ (Minnich et al., 2009a), resulting in ZT improvements over their bulk counterparts. Unlimited to traditional TE materials, the nanostructuring approach may also yield a high ZT in materials that were previously unsuitable for TE applications due to their high thermal conductivities. This concept was demonstrated in nanostructured bulk silicon, where a ZT around 0.7 was achieved at around 1200 K (Bux et al., 2009). With bulk-like electrical properties and significantly reduced thermal conductivity, ZT=0.6 at room temperature was reported for rough silicon nanowires (Hochbaum, 2008). Low thermal conductivities were also found in silicon nanomesh structures, with electrical conductivities preserved from bulk silicon in the high-doping range (Yu et al., 2010). Along this line, ZT around 0.4 was measured at room temperature for silicon membranes with high density of nanoscopic holes (Tang et al., 2010).
Despite these promising results, very little theoretical work has been conducted to understand the phonon transport in nanostructured bulk materials, which hinders the prediction of their potential ZT improvements. There have been efforts applying the Boltzmann Transport Equation (BTE) to periodic 2D structures (Chung & Kaviany, 2000; Yang & Chen, 2004; Yang et al., 2005; Prasher, 2006; Miyazaki et al., 2006; Pattamattaa & Madnia, 2009), but with the gray medium approximation, i.e., a frequency-independent phonon mean free path (MFP). For arbitrary structures, Monte Carlo (MC) simulations are

more favorable to solving the BTE. Only considering the boundary scattering of phonons, MC simulations were first conducted to understand the 1D thermal-conductance measurements on polished single crystals of pure silicon at low temperatures (Klitsner et al., 1988). Taking the internal collisional processes of phonons into account, Peterson designed a MC scheme based on the gray-medium approximation to study 1D heat transfer problems (Peterson, 1994). More recently, the MC technique was applied to 2D nanowire composites (Jeng et al., 2008; Tian & Yang, 2007) and 3D nanoparticle composites (Jeng et al., 2008). The work by Jeng et al. was the first phonon MC simulations for a composite system. Nevertheless, the gray-medium approximation employed in both studies could lead to a significant underestimation of phonon size effects inside micro- to nano-structured bulk materials. For example, experimental results have suggested strong phonon size effects in micro-porous silicon films (Song & Chen, 2004), which can be explained only if frequency-dependent phonon MFPs are considered (Hao et al., 2009). With advancements of theoretical and numerical tools (McGaughey & Kaviany, 2005; Broido et al., 2007; Lindsay & Broido, 2008; Henry & Chen, 2008; Turney et al., 2009), more accurate information on phonon MFPs for some materials are becoming available. Such advancements call for the development of numerical tools that can include the frequency dependence of phonon transport (Narumanchi et al., 2006).

In this chapter, a MC simulation technique considering frequency-dependent phonon MFPs is introduced to investigate the phonon transport in various periodic structures. A novel boundary condition based on the periodic heat flux with a constant virtual wall temperature is developed for the studied periodic structures. This allows us to calculate the thermal conductivity of a periodic structure with a single period as the computational domain. In the literature, frequency-dependent phonon MC simulations were first performed on solid thin films (Mazumder & Majumdar, 2001). However, the suggested treatment for three-phonon scattering, including normal process (N process) and Umklapp process (U process), violated energy conservation before and after the three-phonon scattering events and thus led to errors in simulations. To correct this, three-phonon scattering treatment respecting the energy conservation was proposed later (Lacroix et al., 2005; Chen et al., 2005; Hao et al., 2009). Unlimited to thin films, the MC simulations were also carried out for nanowires (Chen et al., 2005; Lacroix et al., 2006; Randrianalisoa & Baillis, 2008) or 1D transient phonon transport in bulk materials (Lacroix et al., 2005). Among all listed studies, the N process and U process were mostly treated together by a combined scattering rate except for that Chen et al. adopted a genetic algorithm to satisfy both energy and momentum conservation for the N process and energy conservation for the U process (Chen et al., 2005). As an extension, our work introduced in this chapter is the first attempt to apply the MC method to complicated geometries with inclusion of frequency-dependent phonon scattering. The simulation code is used to compute the lattice thermal conductivities of 2D porous silicon with periodically aligned pores (Hao et al., 2009) and 3D silicon nanoparticle composites (Hao et al., 2010). The latter one is essentially nano-grained bulk silicon.

For lightly doped silicon, frequency-dependent MC simulations show that a large thermal conductivity reduction can be observed even in micro-porous structures, an effect that is not expected if an average phonon MFP is used. This indicates that phonon size effects in lightly doped nanostructured bulk silicon can be significantly underestimated if frequency-dependent phonon MFPs are not included into the model.

For heavily doped silicon nanocomposites used for thermoelectrics, phonons are strongly scattered by charge carriers and point defects inside the grains. In analyzing the

experimental data of n-type silicon nanocomposites with grain sizes around 200 nm, we find that grain interface scattering of phonons is negligible and much smaller grain sizes are required to obtain remarkable phonon size effects. Based on the parameters extracted from fitting experimental results, we predict a ZT around 1.0 at 1173 K as grain sizes are reduced to 10 nm. This ZT value is comparable to traditional SiGe bulk alloys and can be further improved by optimizing electrical properties. Compared to other TE materials using exotic and expensive elements, pure silicon nanocomposites have significant advantages for commercialization in terms of cost and material abundance.

Unlimited to 2D porous silicon and 3D silicon nanocomposites, MC simulations can also be applied to other materials with various structures and geometries. The work demonstrated in this book chapter sets up the platform for lattice thermal conductivity predictions across a wide range of length scales.

2. Basic simulation scheme

In a MC simulation, phonons bundles are first drawn and distributed randomly across the computational domain. Each bundle represents a number of phonons with similar properties. Their initial states (velocity, frequency, branch, and traveling direction) are generated by a random sampling approach based on the equilibrium phonon spectrum (Mazumder & Majumdar, 2001; Chen et al., 2005), which will be discussed later. With their individual velocities and traveling directions, phonons are allowed to move and may experience various scattering events during their movement. At each time step, whether a phonon will get scattered and thus change its state is determined by a random number and the individual scattering probabilities. By tracking a large number of phonons and averaging the results over a long period of time, statistically the MC simulations will approach the BTE solutions after convergence.

As an overview, the procedure of MC simulations is briefly described here. We still follow the schematic process flow given in the previous work (Jeng et al., 2008), but the gray-medium approximation is replaced by the frequency-dependent model. In the simulation, the computational domain is divided into many spatial bins, also called subcells. Because it is not feasible to simulate a large number of phonons, phonons are grouped into bundles (with W phonons per bundle) to save computer memory. States of phonons inside each bundle are identical, i.e., they share the same angular frequency ω, traveling direction $\vec{k}$, polarization p, and group velocity $V_{g,p}(\omega)$, where the subscript p indicates the polarization. In this chapter, only the longitudinal acoustic (LA) branch and two transverse acoustic (TA) branches will be considered because the optical branches contribute little to the thermal conductivities directly (Chen, 2005). The potential effect of optical phonon scattering on the acoustic phonon MFPs (Lindsay & Broido, 2008) is included via the molecular dynamics simulation results themselves (Henry & Chen, 2008), from which phonon MFPs are obtained for our MC simulations.

At the beginning of each simulation, phonon bundles are generated inside the computational domain according to the initial temperatures assigned to individual subcells. The states of created phonons are randomly sampled based on the equilibrium phonon spectrum $\langle n \rangle D(\omega)$ (Mazumder & Majumdar, 2001; Chen et al., 2005), where $D(\omega)$ is the density of states for phonons, $\langle n \rangle$ is the Bose-Einstein distribution at the current subcell temperature T, defined as

$$\langle n \rangle = \frac{1}{\exp\left(\frac{\hbar\omega}{k_B T}\right) - 1}. \tag{1}$$

For a subcell with volume V_{sub}, the number of created phonon bundles is $V_{sub}\sum_{p=1}^{3}\int_0^{\omega_{p,\max}} \langle n \rangle D(\omega)\, d\omega / W$, in which $\omega_{p,\max}$ is the maximum phonon frequency for branch p, and W is again the phonon bundle size. Initially, the created phonon bundles are randomly distributed spatially inside each subcell. In all simulations, W is chosen so that the total number of initialized phonon bundles inside the whole domain is less than 1.5×10^7. Although smaller W is always preferred for less fluctuations in simulation results, the computing speed can be extremely slow with more phonon bundles in the domain. To define the frequency of a phonon bundle, ω_0, a random number R ($0 \le R \le 1$) is generated and ω_0 value should satisfy

$$R = \frac{\sum_{p=1}^{3}\int_0^{\omega_0} \langle n \rangle D(\omega)\, d\omega}{\sum_{p=1}^{3}\int_0^{\omega_{p,\max}} \langle n \rangle D(\omega)\, d\omega}. \tag{2}$$

The exact polarization of the phonon is determined by another random number between zero and unity. It indicates the LA branch if the number is less than the ratio

$$P = \left.\frac{\left[\langle n \rangle D(\omega)\right]_{LA}}{2\left[\langle n \rangle D(\omega)\right]_{TA} + \left[\langle n \rangle D(\omega)\right]_{LA}}\right|_{\omega=\omega_0}, \tag{3}$$

in which $\left[\langle n \rangle D(\omega)\right]_{LA}$ and $\left[\langle n \rangle D(\omega)\right]_{TA}$ represent the product $\langle n \rangle D(\omega)$ for the LA branch and TA branch, respectively. Otherwise, the phonon bundle belongs to a TA branch. After the polarization and angular frequency of a phonon bundle are both determined, its group velocity $V_{g,p}(\omega)$ can be obtained from the phonon dispersion curve. For the 3D simulation, the traveling direction of a phonon is generated by two random numbers, R_1 and R_2 ($0 \le R_{1,2} \le 1$). The unit vector of the traveling direction is

$$\vec{k} = \begin{pmatrix} \sin\theta\cos\psi \\ \sin\theta\sin\psi \\ \cos\theta \end{pmatrix}, \tag{4}$$

where the polar angle θ satisfies $\cos\theta = 2R_1 - 1$, and the azimuthal angle ψ is determined by $\psi = 2\pi R_2$.

Within a time step, each phonon bundle travels with its own group velocity, which is $V_{g,L}(\omega)$ for the longitudinal mode and $V_{g,T}(\omega)$ for the transverse mode. To achieve good spatial resolutions, the time step Δt is chosen so that the maximum travel distance of a phonon bundle within Δt, $V_{\max}\Delta t$, is smaller than the subcell dimension. Consequently, phonon bundles will generally take a few time steps to travel out of a subcell, which enables us to better capture the phonon movement. During their travels, the phonons may

encounter the interfaces or the domain boundaries, and will change their trajectories. The interface transport treatment will be discussed in the following subsections.
After the phonon movement, the total phonon energy inside each subcell is calculated and divided by the subcell volume to get the phonon energy density, defined as

$$E = \sum_{p=1}^{3} \int_0^{\omega_{p,\max}} \hbar\omega \langle n \rangle D(\omega) d\omega , \tag{5}$$

in which the pseudo-temperature $\tilde{T}$ of a subcell appears in the term

$$\langle n \rangle = \frac{1}{\exp\left(\dfrac{\hbar\omega}{k_B \tilde{T}} \right) - 1} , \tag{6}$$

and $\tilde{T}$ can be computed by the numerical inversion of Eq. (5) (Mazumder & Majumdar, 2001; Chen et al., 2005; Hao et al., 2009). The above expression works for phonons in equilibrium, but becomes invalid when we deal with transport processes. Within an infinitesimal time step Δt, the density of scattered phonons can be expressed as

$$N_s = \sum_{p=1}^{3} \int_0^{\omega_{p,\max}} \frac{\Delta t}{\tau(\omega)} \langle n \rangle D(\omega) d\omega , \tag{7}$$

where $\tau(\omega)$ is the scattering relaxation time, the weight $\Delta t / \tau(\omega)$ is the probability of being scattered, the subscript s indicates scattered phonons. Similarly, the energy density of scattered phonons is

$$E_s = \sum_{p=1}^{3} \int_0^{\omega_{p,\max}} \hbar\omega \frac{\Delta t \langle n \rangle}{\tau(\omega)} D(\omega) d\omega , \tag{8}$$

instead of the energy density E in Eq. (5). For a fixed time step Δt, we can always use

$$\frac{E_s}{\Delta t} = \sum_{p=1}^{3} \int_0^{\omega_{p,\max}} \hbar\omega \frac{\langle n \rangle}{\tau(\omega)} D(\omega) d\omega \tag{9}$$

to evaluate the temperature of scattered phonons, denoted as T_S. In thermal equilibrium, T_S is equal to the subcell temperature $\tilde{T}$ though T_S is only sampled among all scattered phonons inside a subcell.
The above approach is consistent with the results from the BTE. Under the relaxation time approximation, the phonon BTE can be written as (Goodson et al., 1997)

$$\frac{\partial f}{\partial t} + V_{g,p}(\omega) \vec{k} \cdot \nabla_{\vec{r}} f = -\frac{f - \langle n \rangle}{\tau(\omega)} , \tag{10}$$

where $\vec{k}$ is the unit vector of the traveling direction, $\langle n \rangle$ is the Bose-Einstein distribution, $\tau(\omega)$ is the scattering relaxation time, vector $\vec{r}$ is the phonon position, f is the phonon distribution function, $V_{g,p}(\omega)$ is the group velocity, and subscript p indicates the polarization. We multiply both sides of Eq. (10) by $\hbar\omega D(\omega)$ and integrate with respect to phonon angular frequency ω. The summation over the three acoustic branches yields

$$\sum_{p=1}^{3}\int_0^{\omega_{p,\max}}\frac{\partial f}{\partial t}\hbar\omega D(\omega)\,d\omega+\sum_{p=1}^{3}\int_0^{\omega_{p,\max}}\hbar\omega D(\omega)V_{g,p}(\omega)\vec{k}\cdot\nabla_{\vec{r}}f d\omega=-\sum_{p=1}^{3}\int_0^{\omega_{p,\max}}\hbar\omega D(\omega)\frac{f-\langle n\rangle}{\tau(\omega)}d\omega \quad (11)$$

On the other hand, phonon energy conservation requires

$$\frac{\partial u}{\partial t}+\nabla_{\vec{r}}\cdot\vec{q}=0\,, \quad (12)$$

in which $u=\sum_{p=1}^{3}\int_0^{\omega_{p,\max}} f\hbar\omega D(\omega)\,d\omega$ is the phonon energy density, and the vector $\vec{q}=\sum_{p=1}^{3}\int_0^{\omega_{p,\max}}\hbar\omega D(\omega)V_{g,p}(\omega)\vec{k}\,f d\omega$ is the heat flux. For the equilibrium situation, u is equalized to E defined in Eq. (5) to get the pseudo-temperature $\tilde{T}$ appearing in $\langle n\rangle$. However, this is not the case when we are only concerned with the scattered phonons. In Eq. (12), it can be observed that

$$\frac{\partial u}{\partial t}=\frac{\partial}{\partial t}\left[\sum_{p=1}^{3}\int_0^{\omega_{p,\max}} f\hbar\omega D(\omega)\,d\omega\right]=\sum_{p=1}^{3}\int_0^{\omega_{p,\max}}\frac{\partial f}{\partial t}\hbar\omega D(\omega)\,d\omega\,, \quad (13)$$

and

$$\nabla_{\vec{r}}\cdot\vec{q}=\sum_{p=1}^{3}\int_0^{\omega_{p,\max}}\hbar\omega D(\omega)V_{g,p}(\omega)\vec{k}\cdot\nabla_{\vec{r}}f d\omega\,. \quad (14)$$

Comparing Eqs. (11) and (12), we obtain

$$\sum_{p=1}^{3}\int_0^{\omega_{p,\max}}\hbar\omega D(\omega)\frac{f-\langle n\rangle}{\tau(\omega)}d\omega=0\,,$$

or

$$\sum_{p=1}^{3}\int_0^{\omega_{p,\max}}\hbar\omega D(\omega)\frac{f}{\tau(\omega)}d\omega=\sum_{p=1}^{3}\int_0^{\omega_{p,\max}}\hbar\omega D(\omega)\frac{\langle n\rangle}{\tau(\omega)}d\omega\,, \quad (15)$$

which indicates that for scattered phonons the numerical inversion process to get $\tilde{T}_s$ must be associated with $\sum_{p=1}^{3}\int_0^{\omega_{p,\max}}\hbar\omega D(\omega)\frac{\langle n\rangle}{\tau(\omega)}d\omega$ instead of the energy density E defined in Eq. (5). Under the gray-medium approximation, $\tau(\omega)$ is a constant for all the phonons at the same temperature, and Eq. (15) will reduce to the case defined by Eq. (5). For the frequency-dependent model, however, cautions must be taken and Eq. (15) must be used to define the temperature of scattered phonons.

The phonons may also experience internal scatterings during their travels. These scatterings are processed at the end of each time step. The scattering probabilities, used to determine

the occurrence of internal scattering events, are first computed based on the updated subcell temperature $\tilde{T}$, phonon branch, and phonon frequency. The selection rule and detailed treatment of scattered phonons will be given later. Basically the simulation repeats the following procedures after the phonon initialization: phonon movement with possible interface or boundary scatterings, subcell temperature update with the new spatial distribution of phonon bundles, internal scattering treatment inside each subcell. Convergence is achieved when the calculated temperature profile no longer changes with time. After the convergence, the thermal conductivity of the studied structure can be derived from the domain dimension, the heat flowing through the domain, and the temperature difference across the domain.

3. Phonon scattering treatment

In MC simulations, phonon bundles may experience internal scatterings (by impurities, charge carriers, or other phonons) or interface scattering, where charge carrier scattering of phonons are normally neglected for lightly doped samples (Mazumder & Majumdar, 2001). The detailed treatments are discussed below.

3.1 Internal scattering treatment

For internal scatterings, we assume that charge carrier scattering and impurity scattering only randomize the phonon bundle traveling direction, leaving the phonon frequency and velocity unchanged. In contrast, the phonon-phonon scattering, including the N process and U process, will reset all phonon states (its frequency, branch, velocity, and traveling direction) according to the current subcell temperature. This will help establish the thermal equilibrium between the scattered phonon bundle and the local temperature.

The phonon overall lifetime τ_T is calculated using the Matthiessen's rule, $\tau_T^{-1}(\omega) = \tau_I^{-1}(\omega) + \tau_N^{-1}(\omega) + \tau_U^{-1}(\omega) + \tau_{E(H)}^{-1}(\omega)$, where τ_I, $\tau_{E(H)}$, τ_N, τ_U are the relaxation times of impurity scattering, charge carrier scattering (τ_E for electrons, τ_H for holes), for N processes, and U processes, respectively. For lightly doped samples, the term $\tau_E^{-1}(\omega)$ or $\tau_H^{-1}(\omega)$ can be neglected. In Callaway's model (Callaway, 1959), N processes were treated differently from other scattering mechanisms, by adding an associated correction term to the thermal conductivity. However, the refinement work by Holland (Holland, 1963) argued that this correction term would possibly cause more errors and N processes should be treated in exactly the same way as other scattering mechanisms. In this work, we follow Holland's treatment and N processes are simply a scattering mechanism added to other mechanisms. Additionally, the N process and the U process are not differentiated, and a combined relaxation time τ_{NU}, defined as $\tau_{NU}^{-1}(\omega) = \tau_N^{-1}(\omega) + \tau_U^{-1}(\omega)$, will be used. The probability for a phonon bundle to be scattered is given by $P(\omega) = 1 - \exp(-\Delta t / \tau_T(\omega))$ (Mazumder & Majumdar, 2001; Hao et al., 2009). For an infinitesimal Δt, $P(\omega)$ simply becomes the weight $\Delta t / \tau_T(\omega)$ in Eqs. (7) and (8). At the end of every time step, a random number R_s ($0 \le R_s \le 1$) is generated for each phonon bundle at a frequency ω_0 and compared with $P(\omega_0)$. The phonon bundle is scattered if R_s is less than $P(\omega_0)$. If a phonon bundle is scattered, another random number R_{NU} will be generated and compared with $P_{NU}(\omega_0) = \tau_{NU}^{-1}(\omega_0) / \tau_T^{-1}(\omega_0)$. The phonon will have phonon-phonon scattering if R_{NU} is less than $P_{NU}(\omega_0)$. Otherwise, it will be scattered by either charge carriers or impurities, which will only randomize its traveling direction.

Phonon-phonon scattering will reset all the states of a phonon bundle, which follows similar procedures as described by Eqs. (2) to (4). However, the spectrum $\langle n \rangle D(\omega)$ in Eqs. (2) and (3) should be replaced by $\langle n \rangle D(\omega)/\tau_{NU}(\omega)$ introduced in Eqs. (7) to (9). Because $1/\tau_{NU}(\omega)$ monotonically increases with ω, most phonons scattered are from the high-frequency portion of the phonon spectrum. As a result, at a fixed temperature the averaged frequency of the phonons scattered by other phonons,

$$\langle \omega \rangle_s = \frac{\sum_{p=1}^{3} \int_0^{\omega_{p,\max}} \frac{1}{\tau_{NU}(\omega)} \hbar\omega \langle n \rangle D(\omega) d\omega}{\sum_{p=1}^{3} \int_0^{\omega_{p,\max}} \frac{1}{\tau_{NU}(\omega)} \hbar \langle n \rangle D(\omega) d\omega}, \tag{16}$$

is higher than the averaged frequency of all the phonons at the same temperature, given as

$$\langle \omega \rangle_{eq} = \frac{\sum_{p=1}^{3} \int_0^{\omega_{p,\max}} \hbar\omega \langle n \rangle D(\omega) d\omega}{\sum_{p=1}^{3} \int_0^{\omega_{p,\max}} \hbar \langle n \rangle D(\omega) d\omega}. \tag{17}$$

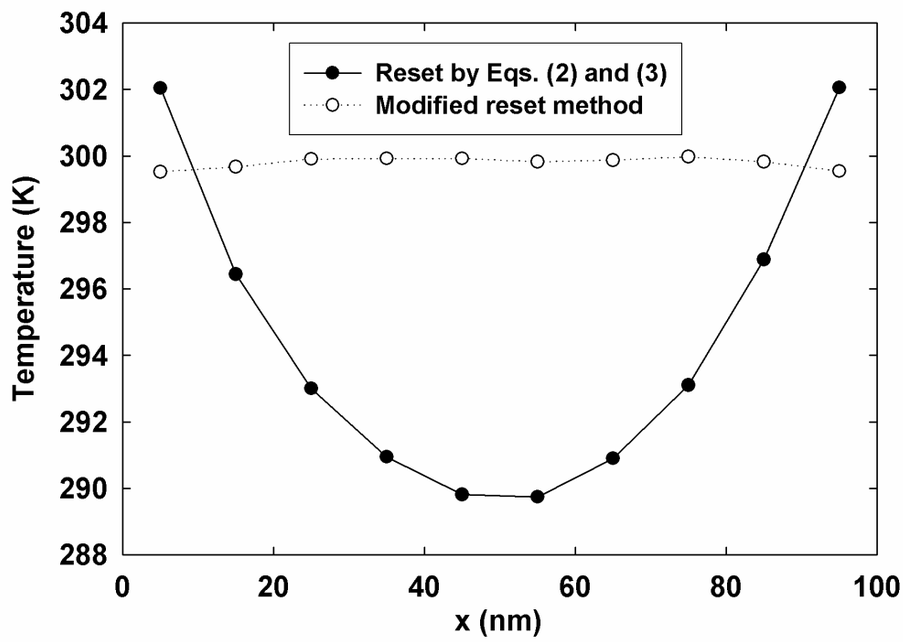

Fig. 1. Calibration of the reset methods for scattered phonons (Hao et al., 2009). The slight asymmetry and undulation of the temperature profiles are attributed to the numerical errors of MC simulations. The 1D computational domain is 100 nm in length and its both ends are fixed at 300 K. The reset method based on Eqs. (2) and (3) always yields an abnormal temperature profile, which can be resolved by replacing the spectrum $\langle n \rangle D(\omega)$ with $\langle n \rangle D(\omega)/\tau_{NU}(\omega)$ in Eqs. (2) and (3). Here the time step is fixed at 1 ps and the temperature of each subcell is averaged over 0.5 ns.

In the literature, Eqs. (2) and (3) were used to reset the states of a scattered phonon bundle (Mazumder & Majumdar, 2001). The phonon bundles experiencing phonon-phonon scattering are assigned frequencies averaged at $\langle\omega\rangle_{eq}$. We find that this treatment will result in a final phonon spectrum distorted from the real spectrum and will yield abnormal temperature profiles when the temperature difference across the domain is small. A simple test can be conducted with the equilibrium situation in which the 1D computational domain has both ends fixed at 300 K (isothermal wall boundary condition in Mazumder & Majumdar, 2001). To simplify, the model used in this test only considers the U processes and impurity scattering (Dames & Chen, 2005). The corresponding scattering rates are: $1/\tau_U(\omega) = B_1\nu^2 T\exp(-B_2/T)$ (U process), where ν is the phonon frequency, B_1 = 3.0×10^{-19} s/K, B_2 =210 K; $1/\tau_I(\omega) = A\omega^4$ (impurity scattering), with A =2.4×10^{-45} s^3. The Debye model is used for the phonon dispersion, with $\omega_{LA,\max} = \omega_{TA,\max}$ = 7.06×10^{13} rad·Hz, and the lattice constant a=5.5 Å. Due to the distorted phonon spectrum from the equilibrium one, the resulting temperature profile always shows a valley in the middle (solid circles in Fig. 1), with a significantly increased number of phonon bundles from equilibrium. This problem is resolved when we use the spectrum $\langle n\rangle D(\omega)/\tau_{NU}(\omega)$ instead of $\langle n\rangle D(\omega)$ in Eqs. (2) and (3) to reset the scattered phonon states (empty circles in Fig. 1). This treatment is consistent with Eq. (15), obtained from the BTE under the relaxation time approximation.

After processing all internal scatterings inside one single subcell, phonons will be either randomly created according to the spectrum $\langle n\rangle D(\omega)$ in Eqs. (2) and (3) or deleted from the domain. Our purpose is to assure the subcell energy conservation before and after the scatterings. The energy imbalance inside a subcell is controlled to be less than $\hbar\omega_{TA,\max}/2$.

3.2 Interface scattering treatment

For micro- and nanostructured materials, both the interface scattering and internal scattering can contribute to the thermal resistance of the material. We assume phonons are diffusely scattered at the interfaces. When a phonon bundle encounters an interface during its travel, it will be diffusely transmitted or reflected. For phonons incident from side 1 of the interface, this is determined by a random number P_r ($0 \le P_r \le 1$) and the interface transmissivity T_{12} from side 1 toward side 2 (Tian & Yang, 2007; Jeng et al., 2008; Hao et al., 2009; Hao et al., 2010). The phonon bundle will be transmitted to side 2 if P_r is less than T_{12}. Otherwise, it will be reflected back to side 1. The reflected or transmitted phonon bundles are assigned a new traveling direction, with all other phonon states (velocity, frequency, and branch) unchanged, and hence phonon mode conversion is not included. For rectangular subcells, the direction reassignment within the anticipated semi-sphere for either reflection or transmission is simple. Equation (4) is again used to generate a direction vector $\vec{k}$ and then the sign of one particular component in $\vec{k}$ will be specified. It should be noted that θ should be determined by $\sin^2\theta = R_1$ instead of $\cos\theta = 2R_1 - 1$ in this case (Jeng et al., 2008). Suppose a phonon bundle moving in the positive x direction is transmitted across a y-z plane interface. It will have a positive x component in its new traveling vector $\vec{k}$. If it is reflected, the x component will be negative. Similarly, we can treat reflection and transmission on x-y and x-z plane interfaces. After the interface scattering, the phonon bundle will continue its movement with the remaining drift time to finish the current time step.

4. Boundary condition

For a periodic structure, the boundary condition used for the numerical solution of the 2D BTE equation (Yang & Chen, 2004) can be extended to the 3D MC simulation. With a $L_x \times L_y \times L_z$ rectangular computational domain, heat is assumed to flow in the positive x direction. Our chosen unit cell is symmetric in both y and z directions. For such a symmetric structure, phonon bundles hitting the four side walls of the domain are specularly reflected (Tian and Yang, 2007; Jeng et al., 2008; Hao et al., 2009; Hao et al., 2010). If the unit cell structure is asymmetric in the y or z directions, we can use periodic boundary conditions for the corresponding side walls. In this case, phonon bundles exiting from the domain on one side wall will re-enter the domain from the same interception position on the opposite side wall, and continue their travels. In the x direction, the essence of the boundary condition is that on both ends of the simulation domain, which we will call the hot and cold walls, the distortions of the distribution functions from the equilibrium distribution are periodic (shown in Fig. 2). This can be written as

$$f_2^-(\theta,\psi,\omega,y,z) - \langle n(y,z)\rangle_2 = f_1^-(\theta,\psi,\omega,y,z) - \langle n(y,z)\rangle_1, \tag{18}$$

$$f_2^+(\theta,\psi,\omega,y,z) - \langle n(y,z)\rangle_2 = f_1^+(\theta,\psi,\omega,y,z) - \langle n(y,z)\rangle_1, \tag{19}$$

in which f is the distribution function, θ is the polar angle, ψ is the azimuthal angle, the subscript "2" donates the cold wall ($x = L_x$) and "1" represents the hot wall ($x = 0$), the superscripts "+" and "-" represent the distribution in the positive and negative x directions. Here $\langle n(y,z)\rangle_1$ and $\langle n(y,z)\rangle_2$ are evaluated at the corresponding local wall temperatures. They are not periodic since their difference is the driving force for heat flow along the x direction.

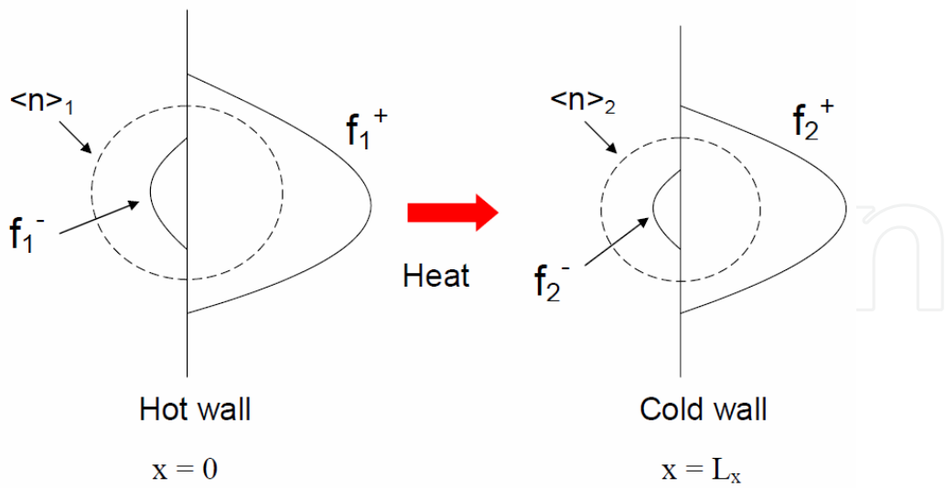

Fig. 2. Distribution functions on the domain boundaries described by the periodic heat flux boundary condition. The hot wall and cold wall positions are located at $(0,y,z)$ and (L_x,y,z), respectively. The equilibrium distributions, $\langle n(y,z)\rangle_1$ and $\langle n(y,z)\rangle_2$, are both isotropic. With the x-direction heat flow, the distribution function f is anisotropic and distorted from $\langle n(y,z)\rangle$.

Equation (18) means when a phonon bundle, following the distribution function $f_1^-(\theta,\psi,\omega,y,z)$, encounters the hot wall during its movement, it will be "absorbed" by the wall. At the same time, a new phonon bundle, following the distribution function $f_2^-(\theta,\psi,\omega,y,z)$, will be emitted from the cold wall to maintain the heat flow through the domain. Similarly, Eq. (19) relates the distribution functions of phonon bundles "absorbed" by the cold wall and phonon bundles emitted from the hot wall. In our simulations, the absorbed phonons are recorded during tracking the phonon movement in each time step. The states of the emitted phonons are determined by Eqs. (18) and (19), as described below.

4.1 Cold wall emission

In Eq. (18), $f_2^-(\theta,\psi,\omega,y,z)$ represents the distributions of phonons entering the simulation domain through the cold wall, which we call cold wall emitted phonons. The distribution of these emitted phonons is determined by $f_1^-(\theta,\psi,\omega,y,z)$, the distributions of phonons leaving the domain from the hot wall, or absorbed phonons. In the y-z plane, a fixed cross section area A is assigned for all subcells. Denoting unit vector $\vec{n}$ as the normal of the wall, $\vec{k}$ as the phonon traveling direction, we multiply $\left(V_{g,p}(\omega)\vec{k}\cdot\vec{n}\right)D(\omega)A\Delta t$ to both sides of Eq. (18) and integrate with respect to ω, and ψ, θ for 2π solid angle. Summation over the three acoustic branches and rearranging the equation yields

$$N_2^-(y,z)=N_1^-(y,z)-\frac{1}{4W}\sum_{p=1}^{3}\int_0^{\omega_{p,\max}}V_{g,p}(\omega)D(\omega)A\Delta t\left(\left\langle n(y,z)\right\rangle_1-\left\langle n(y,z)\right\rangle_2\right)d\omega, \quad (20)$$

where W is the number of phonons in each bundle, $N_1^-(y,z)$ is the number of locally absorbed phonon bundles on the hot wall, $N_2^-(y,z)$ is the number of phonon bundles locally emitted by the cold wall. Similarly, multiplying $\hbar\omega\left(V_{g,p}(\omega)\vec{k}\cdot\vec{n}\right)D(\omega)A\Delta t$ to both sides of Eq. (18) and conducting similar procedures yields

$$Q_2^-(y,z)=Q_1^-(y,z)-\frac{1}{4W}\sum_{p=1}^{3}\int_0^{\omega_{p,\max}}\hbar\omega V_{g,p}(\omega)D(\omega)A\Delta t\left(\left\langle n(y,z)\right\rangle_1-\left\langle n(y,z)\right\rangle_2\right)d\omega, \quad (21)$$

in which $Q_2^-(y,z)$ is the total phonon bundle energy locally emitted from the cold wall for area A, $Q_1^-(y,z)$ is the total phonon bundle energy absorbed by the hot wall.

In our simulations, all the $N_1^-(y,z)$ phonon bundles are deleted from the domain but their states are separately stored as a pool for the cold wall emission. The phonon states include its frequency, velocity, location intercepting the wall, the remaining drift time after hitting the wall, and its traveling direction. To obtain the $N_2^-(y,z)$ phonon bundles, we need to delete

$$N_{del}=\frac{1}{4W}\sum_{p=1}^{3}\int_0^{\omega_{p,\max}}V_{g,p}(\omega)D(\omega)A\Delta t\left(\left\langle n(y,z)\right\rangle_1-\left\langle n(y,z)\right\rangle_2\right)d\omega, \quad (22)$$

phonon bundles from the pool consisting of $N_1^-(y,z)$ phonon bundles. To do this, N_{del} phonons are first randomly generated according to the spectrum $V_{g,p}(\omega)D(\omega)\left(\left\langle n(y,z)\right\rangle_1-\left\langle n(y,z)\right\rangle_2\right)$, which replaces $\langle n\rangle D(\omega)$ in Eqs. (2) and (3) for phonon state determination in this situation. Among the $N_1^-(y,z)$ phonon bundles, we delete N_{del}

bundles that best match the frequencies and branches of the generated bundles. The states of these N_{del} bundles are saved for later usage, which will be clear when the hot wall emission is discussed. The phonons left in the pool constitute the $N_2^-(y,z)$ phonons emitted from the cold wall.

4.2 Hot wall emission

Similar to Eq. (20), the hot wall emission can be derived from Eq. (19) as

$$N_1^+(y,z) = N_2^+(y,z) + \frac{1}{4W}\sum_{p=1}^{3}\int_0^{\omega_{p,\max}} V_{g,p}(\omega)D(\omega)A\Delta t\left(\left\langle n(y,z)\right\rangle_1 - \left\langle n(y,z)\right\rangle_2\right)d\omega, \quad (23)$$

in which $N_2^+(y,z)$ phonon bundles are absorbed by the cold wall, and they are known for each time step. The previous N_{del} phonon bundles deleted from the cold wall emission pool, with their traveling directions reversed this time, will be added to the $N_2^+(y,z)$ bundles and thus form the $N_1^+(y,z)$ bundle pool for the hot wall emission.

4.3 Periodic heat flux with a constant virtual wall temperature boundary condition

Based on the foregoing discussions, a novel periodic heat flux with a constant virtual wall temperature boundary condition can be introduced for periodic structures. We assign $T_1(y,z) \equiv T_h$ to the hot wall and $T_2(y,z) \equiv T_c$ to the cold wall of the domain. By combining such temperature setting with periodic boundary conditions used in Eqs. (18) and (19), the local heat flux $q"$ is allowed to vary across each virtual wall but still hold its periodicity, $q"(0,y,z) = q"(L_x,y,z)$. It should be noted that our boundary condition is fundamentally different from the traditional isothermal wall boundary condition (Mazumder & Majumdar, 2001). In the latter case, the computational domain is sandwiched between two physical black walls. For a periodic structure, the isothermal wall boundary condition requires a computational domain consisting of many periods to eliminate the strong end effects. The exact thermal conductivity can be obtained only if the calculation results will no longer change with further increasing the number of periods inside the computational domain. In contrast, our boundary condition is specified on two "virtual" walls cut arbitrarily inside the material without affecting the real heat flow, as long as the virtual walls define an integer multiple of unit cells of the periodic structure. In principle, accurate thermal conductivities can be obtained using a single period as our computational domain. This will significantly reduce the computational cost. Our calculation validates this point.

5. Results and discussion

The previous sections cover the basic simulation procedure, the treatment of different phonon scatterings, and the employed boundary condition for a periodic structure. With these, we are ready to use frequency-dependent MC simulations to investigate the phonon transport in various periodic structures. My calculations here are focused on silicon-based materials, including 2D micro- to nano-porous silicon and 3D silicon nanocomposites.

5.1 Employed models for different scattering mechanisms

To get dependable simulation results, it is necessary to use accurate frequency-dependent phonon lifetimes in silicon. In the literature, Holland's model (Holland, 1963) provided a

very good fit to the experimental data from 1.7 to 1300 K. However, in his work the real phonon dispersion was simplified as two linear sections for both TA and LA branches, resulting in abrupt changes of phonon group velocities across the threshold frequencies between two linear sections (ω_1 for two TA branches, ω_4 for the LA branch). In addition, the phonon-phonon scattering rates employed different expressions for the TA branches below and above ω_1. As a result, the calculated phonon MFPs had a significant jump across the threshold frequencies. Although the first problem was fixed using the real phonon dispersion (Mazumder & Majumdar, 2001), the second issue still remained and led to a TA phonon MFPs jump from 9 nm to 179 nm at ω_1 for Si. Henry and Chen carried out molecular dynamics simulations to study the spectral dependence of phonon MFPs in silicon (Henry & Chen, 2008). The results of this past work are now incorporated into the MC simulations. Based on their calculations from 300 to 1000 K, the combined relaxation time for the N and U processes follows the expression $\tau_{NU} = A_{NU}\nu^{-2}T^{-b}$, where ν (in Hz) is the phonon frequency, $A_{NU} = 5.32\times10^{18}$ K$^{1.49}$/s, b= 1.49 for LA phonons; and $A_{NU} = 5.07\times10^{18}$ K$^{1.65}$/s, b =1.65 for TA phonons. To simplify the simulation, an isotropic phonon dispersion is assumed and the calculated (001) direction phonon dispersion is used to evaluate the frequency-dependent phonon group velocity and density of states. The whole phonon spectrum (from 0 to $\omega_{LA,\max}$) is discretized into N_b equally spaced intervals. Numerical integrations with respect to the phonon frequency, such as the evaluation of Eq. (5), are all conducted by summing the integrals over all N_b intervals, in which the integrals are evaluated at the central frequency of each interval.

For doped bulk silicon, the impurity-phonon scattering should be considered in addition to the phonon-phonon scattering. The phonon scattering rate by impurities is expressed as (Klemens, 1955)

$$\tau_I^{-1}(\omega) = A\omega^4, \tag{24}$$

where the constant $A = A_{\delta M} + A_{\delta R} + A_x$ (Asheghi et al., 2002). Here $A_{\delta M}$, $A_{\delta R}$, A_x correspond to the scattering due to the presence of impurity atoms, the induced strain by inserting impurity atoms into the lattice, and unintentional impurities and imperfections, respectively. The employed phonon dispersion suggests an average sound velocity as $v_s = \left\{\left[2v_{TA}^{-1} + v_{LA}^{-1}\right]/3\right\}^{-1}$ =6127 m/s and this v_s is used to compute $A_{\delta M}$ and $A_{\delta R}$. All other parameters are unchanged from the previous work that uses v_s =6400 m/s instead (Asheghi et al., 2002).

For free charge carrier scatterings of phonons (only considered for heavily doped samples), the scattering rate is given as (Ziman, 1956 & 1957)

$$\tau_E^{-1}(\omega) = \frac{E_d^2 m^{*3} v_g}{4\pi\hbar^4 d}\frac{k_B T}{\frac{1}{2}m^* v_g{}^2} \times\left\{\frac{\hbar\omega}{k_B T} - \ln\frac{1+\exp\left[\left(\frac{1}{2}m^* v_g{}^2 - E_F\right)/k_B T + \hbar^2\omega^2/8m^* v_g{}^2 k_B T + \hbar\omega/2k_B T\right]}{1+\exp\left[\left(\frac{1}{2}m^* v_g{}^2 - E_F\right)/k_B T + \hbar^2\omega^2/8m^* v_g{}^2 k_B T - \hbar\omega/2k_B T\right]}\right\}, \tag{25}$$

where T is the absolute temperature, $\hbar$ is the Planck constant, k_B is the Boltzmann constant, E_d is the acoustic deformation potential, m^* is the density of states effective mass, d is the density, v_g is the averaged phonon group velocity, and E_F is the Fermi energy calculated by the generalized Kane's model based on the carrier concentration (Kane, 1957; Kołodziejczak, 1961). Because the investigated silicon nanocomposites always have a carrier concentration much higher than the carrier concentration threshold 3.0×10^{18} cm^{-3} for becoming metallic (Yamanouchi et al., 1967; Alexander & Hocomb, 1968), the scattering of phonons by bound electrons or holes will not be considered.

Given the relaxation times of different mechanisms, the lattice thermal conductivity of bulk silicon can be calculated by (Chen, 2005; Holland, 1963)

$$k_L = \frac{1}{3}\sum_{p=1}^{3}\int_0^{\omega_{p,\max}} C_p(\omega)V_{g,p}^2(\omega)\tau_{T,p}(\omega)d\omega\,, \tag{26}$$

where the subscript p indicates the polarization, $C_p(\omega)$ is the spectral volumetric specific heat, $V_{g,p}(\omega)$ is the phonon group velocity, and $\tau_{T,p}(\omega)$ is the overall phonon relaxation time for branch p and frequency ω.

5.2 Calibration for bulk silicon

The MC code developed is first calibrated with bulk silicon and only phonon-phonon scattering is considered. In this case, Eq. (26) predicts bulk k_L=146.5 W/m·K at 300 K. Because we only employ the phonon dispersion along the (001) direction for our calculations, this isotropic k_L value is lower than the prediction averaged in three major crystal directions by Henry and Chen (175 W/m·K by the BTE approach, 166 W/m·K by the Green-Kubo analysis), in which the phonon density of states, used in calculating $C_p(\omega)$, are summed over the Brillouin zone.

With N_b=2000, phonon bundle size W = 2, T_h = 305 K and T_c=295 K are assigned to a rectangular computational domain that is 200 nm in length, and 10 nm ×10 nm for the cross section area. The time step Δt is fixed at 0.6 ps in this simulation. After 1 ns, the temperature profile (averaged over successive 800 time steps) converges and its variation in the following steps is within 0.5 % (Fig. 3). The linearity for the converged temperature profile is R^2=0.9987. The heat flow passing through the domain always fluctuates due to the randomness of phonon absorption by the hot and cold walls at different time steps. This heat flow is obtained by averaging the net heat flows across the two walls, which are $Q_2^+ - Q_2^-$ for the cold wall and $Q_1^+ - Q_1^-$ for the hot wall. After the convergence of the temperature profile, the heat flows at different time steps are further averaged over a period, with the highest and lowest 20 values excluded. To be accurate, the averaging period is chosen to be no shorter than the time for the temperature profile to converge. The lattice thermal conductivity can then be calculated with this averaged heat flow and the temperature difference across the domain. Averaging over a period of 16 ns yields a thermal conductivity of 142.9 W/m·K, which is slightly lower than the expected 146.5 W/m·K. In comparison, averaging the heat flows over any 2.4 ns period after the initial 1 ns gives thermal conductivities ranging from 141.8 to 145.4 W/m·K, all with less than 4% relative error. At 300 K, our employed model predicts that around 53% of the lattice thermal conductivity is contributed by phonons with MFPs larger than the 200 nm domain length. The chances for these phonons to be scattered are relatively small but their contributions can still be included by averaging the results over a long period of time.

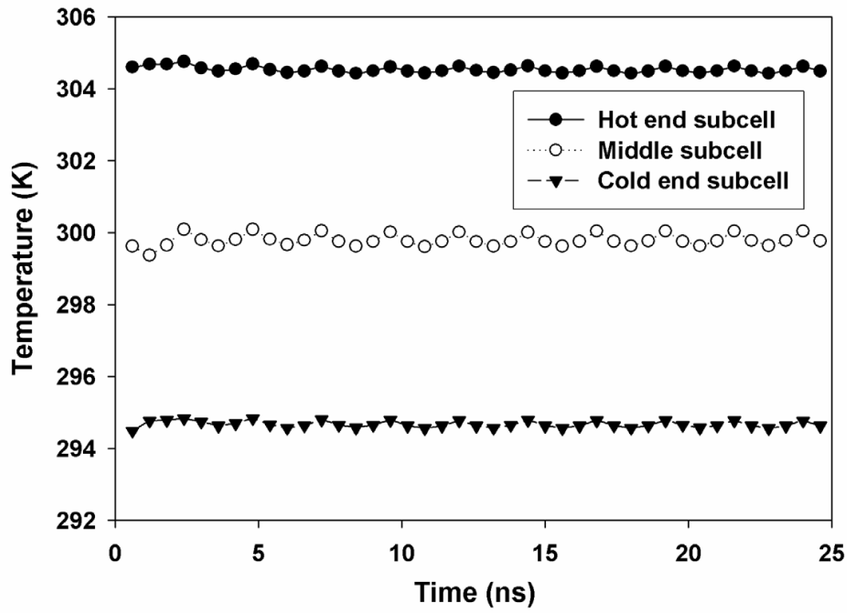

Fig. 3. The time history of subcell temperatures for a pure silicon computational domain (Hao et al., 2009). The 200 nm×10 nm×10 nm domain consists of 20 cubic subcells that are 10 nm in dimension. The subcell adjacent to the hot wall (hot end subcell), the one adjacent to the cold wall (cold end subcell), and the middle one are tracked here. Every temperature point is averaged over the previous 800 time steps, or 0.48 ns.

One important aspect of the statistical MC simulation is the signal-to-noise ratio, which is mainly reflected in the fluctuation of the heat flowing through the domain at different time steps. Such fluctuations can always be decreased by reducing the bundle size. However, this also requires a significantly larger computer memory that is not feasible in many cases. Averaging the heat flow over a longer period of time can be used to compensate the errors brought by large bundle sizes but requires more computational time. In practice, a balance between computation time and computer memory usage is required. The temperature difference between the cold wall and the hot wall can be increased to improve the signal-to-noise ratio, mainly by increasing the signal (averaged heat flow). The accuracy of the calculation will be slightly affected because in this case the thermal conductivity is an effective value averaged over a wider temperature range and does not correspond well to a particular temperature.

5.3 Two-dimensional porous silicon with aligned pores

Although it is one of the most important materials in the electronics industry, silicon is unsuitable for some applications because of its high thermal conductivity. Porous silicon, with its much lower thermal conductivity, could provide a simple solution to widen the usage of silicon (Yamamoto et al., 1999; Chung & Kaviany, 2000; Lee et al., 2007; Yu et al., 2010; Tang et al., 2010). Along this line, nanoscale porous structures are expected to introduce strong phonon size effects and further lower the thermal conductivity from the prediction based on the classical Fourier heat conduction theory. Surprisingly, experimental results showed that even microsize periodically arranged through-film pores would still yield notable phonon size effects in silicon thin films (Song & Chen, 2004). This reduction in

thermal conductivity cannot be explained using an averaged phonon MFP that is on the order of a hundred nanometer. To better understand the phonon size effects in porous silicon, we carry out frequency-dependent MC simulations on 2D porous silicon with periodically arranged square pores, in which the pore dimensions range from 5 nm to 2 μm. It is assumed that phonons are all specularly reflected on the z-direction, i.e., the top and bottom surfaces of the film shown in Fig. 4a. This choice of the z-direction boundary condition converts the problem into a 2D case where the z-direction film thickness will not affect the results. The purpose of choosing this boundary condition is to reduce the computational load since a small z-direction dimension can be chosen (1 to 10 nm for all cases). Figure 4b presents the simulated film structure with the chosen computational domain, which is a square-shape period in the x-y plane, with a square pore in its center. All phonons encountering the rough pore boundaries are reflected diffusely. The silicon film is assumed to be n-type with a doping level as 5×10^{15} cm^{-3}. The electronic thermal conductivity is negligible (<0.01 W/m·K from the Wiedemann-Franz Law) for this low doping level and the electron-phonon scattering can also be neglected. The constant A for impurity scattering is determined as 9.3×10^{-50} s^3, with A_x as zero for slightly doped samples (Asheghi et al., 2002).

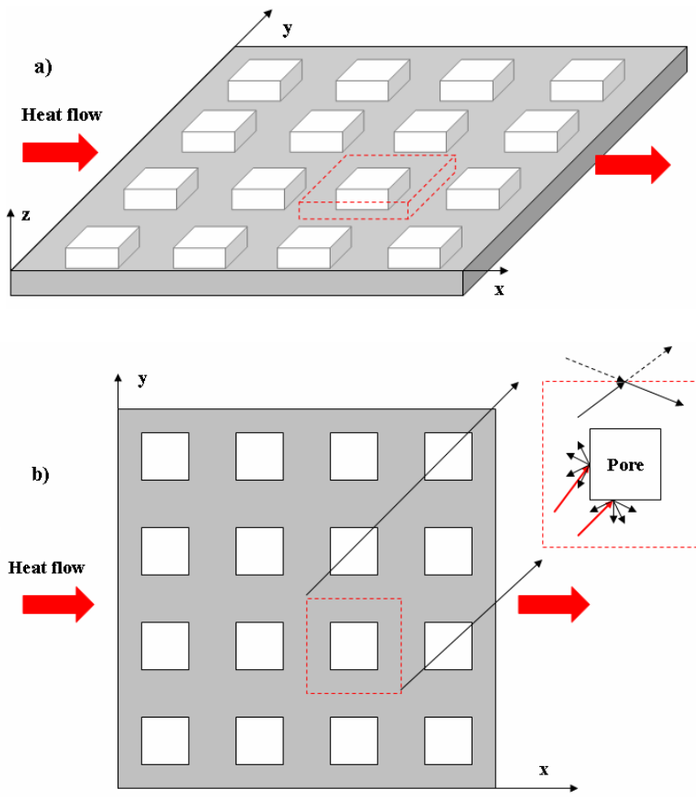

Fig. 4. a) Structure of the simulated porous silicon film. The chosen computation domain (marked by dashed line) is a single period with a square pore right in its center. b) Top view of the film, with details of the computational domain.

Based on the used parameters, the corresponding bulk lattice thermal conductivity is slightly reduced to 145.9 W/m·K according to Eq. (26). In our simulations, the period of the

pores always equals twice the square pore size, resulting in a fixed porosity Φ = 0.25. Without considering the phonon size effects, the Eucken model (Eucken, 1932 & 1933) from the Fourier classical heat conduction theory predicts

$$k_{Porous} / k_{Solid} = (1-\Phi)/(1+\Phi/2), \tag{27}$$

for cubic pores, and the calculated k_{Porous} is 97.3 W/m·K.

A 10 K temperature difference is applied to the computational domain for cases with period sizes up to 1 μm. To improve the signal-to-noise ratio, the temperature difference is increased to 20 K for larger period sizes. The normalized temperature contour for the 200-nm-period case is shown in Fig. 5a, with subcells chosen as 5 nm cubes. The normalization is performed as $(T-T_{\min})/(T_{\max}-T_{\min})$, where T is the subcell temperature, and the subscripts max and min denote the maximum and minimum temperatures of subcells. Figure 5b presents the x-direction normalized temperature distribution at a few typical y locations. When the spacing between adjacent pores is smaller than the phonon MFPs, ballistic phonon transport becomes more important compared with the internal phonon scatterings inside silicon. Therefore, close to the left surface of the pore (facing the incoming heat flow) there will be a locally heated region because it receives hotter phonons directly from the "upstream" adjacent pore. Similarly, a locally cooled region will exist close to the back surface of the pore. In both cases, we will have a negative local temperature gradient compared with the main x-direction temperature gradient across the whole domain. These local "overshoots" do not violate the second law of thermodynamics because no local thermal equilibrium is established under the strong phonon ballistic transport (Yang & Chen, 2004; Jeng et al., 2008).

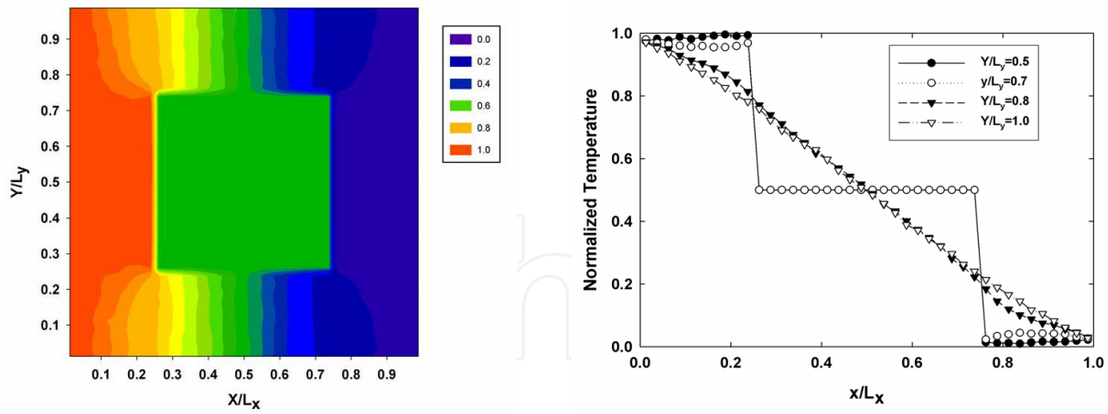

(a) (b)

Fig. 5. (a) Normalized temperature contour for a 200 nm period (Hao et al., 2009). The empty pore region is assigned the average temperature of the domain. (b) Temperature distribution along the x direction for typical y locations.

The room-temperature in-plane lattice thermal conductivities, averaged over at least 4 ns after the convergence of the temperature profile, are plotted as a function of period size in comparison with the Eucken model prediction (Fig. 6). To clearly show the thermal conductivity reduction, all the values are normalized by the bulk thermal conductivity k_{Solid}

(145.9 W/m·K). Remarkable phonon size effects can be observed even for a period size of 4 μm, which is one magnitude larger than the averaged phonon MFP of 119 nm at 300 K. In comparison, solving the BTE based on the gray-medium approximation suggests k_{Porous} / k_{Solid} to be around 0.66 (shown in Fig. 6) for exactly the same 2D unit cell with a phonon Knudsen number of 0.1, where the Knudsen number is defined as the averaged phonon MFP divided by the period size (Miyazaki et al., 2006). Although isothermal wall boundary condition (Mazumder & Majumdar, 2001) is used instead of the periodic heat flux boundary condition to solve the BTE, this comparison clearly shows that phonon size effects cannot be accurately predicted without considering the frequency-dependent phonon MFPs.

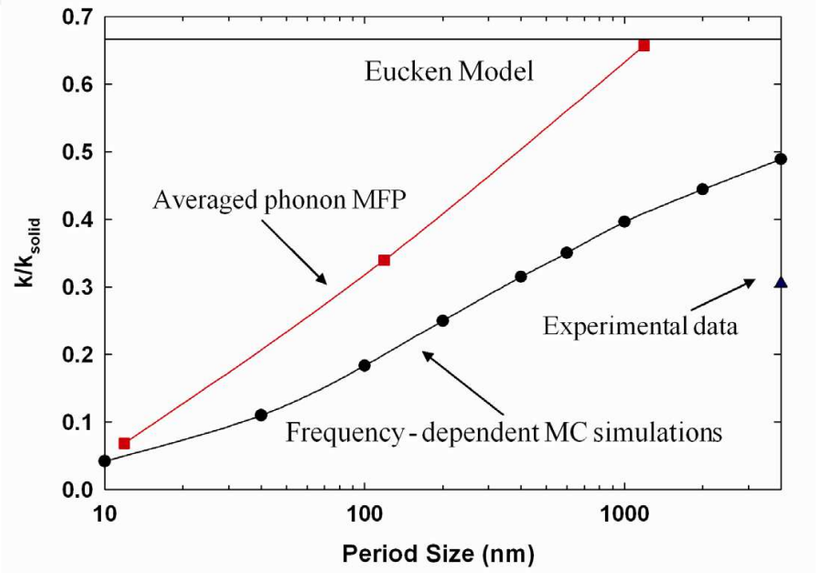

Fig. 6. Normalized in-plane lattice thermal conductivities of porous silicon films as a function of period size (Hao et al., 2009). The circles are the frequency-dependent MC simulation results. The squares are results by solving the BTE for the same 2D unit cell (Miyazaki et al., 2006), with an averaged phonon MFP and isothermal wall boundary condition applied. The triangle is Song's experimental result of a 4.49 μm thick silicon film with similar doping level, 2.3 μm pore diameter, 4 μm pore spacing, and a corresponding porosity Φ = 0.26 (Song & Chen, 2004). The Eucken model prediction (solid line) is plotted for comparison.

Song and Chen reported a 44.5 W/m·K (also shown in Fig. 6) lattice thermal conductivity at 300 K for a 4.49 μm thick silicon film with similar doping level, 2.3 μm pore diameter, 4 μm pore spacing, and a corresponding porosity Φ = 0.26 (Song & Chen, 2004). Our current prediction is still higher than this result, which can be mainly attributed to two factors. First, our simulation is 2D while the phonon scattering at the film top and bottom surfaces are mostly diffuse (Mazumder & Majumdar, 2001). We expect such diffuse scattering should further reduce the thermal conductivity. Secondly, during the process of drilling through-film pores, damaged surface layer may be created by the ion bombardment of the deep reactive-ion etching (Song & Chen, 2004), and effectively increase A_x. The pore shape difference is not expected to be very important because of the phonon diffuse scattering on the pore boundaries and similar porosities. Despite the difference, our simulation shows

that indeed size effects exist even in micron range, consistent with experimental observations. Contribution of long-MFP phonons to the thermal conductivity is significantly suppressed by the scattering of periodically arranged pores, and such influence can be predicted only if frequency-dependent phonon MFPs are considered.

5.4 Silicon nanocomposites

To simulate the phonon transport inside nanocomposites, another critical parameter is the phonon transmissivity across interfaces. The diffuse mismatch model (Swartz, 1989; Chen, 2005) assumes that phonons emitted from an interface cannot tell which side they come from, i.e., $1-T_{12}(\omega)=T_{21}(\omega)$. Here T_{ij} denotes the transmissivity from side i to j. For an interface with the same material on both sides, we have $T_{12}(\omega)=T_{21}(\omega)$ by symmetry and thus $T_{12}(\omega)\equiv 0.5$. At 575 K, an average phonon transmissivity $\langle T\rangle=0.57$ is given by molecular dynamics simulations for silicon grain interfaces (Maiti et al., 1997), which is close to our estimation here.

The studied n-type silicon nanocomposites were synthesized in two steps as described in the literature (Poudel et al., 2008; Ma et al., 2008; Joshi et al., 2008; Wang et al., 2008; Yang et al., 2009; Zhu et al., 2009; Bux et al., 2009). We first prepared nanopowders by high energy ball milling bulk silicon together with the doping element chunks (3% phosphorous in mole). Secondly, we hot-pressed the obtained $Si_{1.00}P_{0.03}$ nanopowders into a bulk disc and measured its TE properties with commercial setups. The ZT of the investigated sample is around 0.55 at 1173 K. The averaged grain size in the sample is determined as 200 nm by transmission electron microscopy. In MC simulations, parameters used for silicon nanocomposites are listed in Table 1. The lattice thermal conductivity k_L is calculated by subtracting the electronic contribution k_e from the measured thermal conductivity (Fig. 7). Here k_e is calculated by the Wiedemann-Franz law, $k_e=L\sigma T$, where L is the computed Lorenz number (Kołodziejczak, 1961), σ is electrical conductivity, and T is absolute temperature. Due to large grain sizes, we do not consider the grain interface influence on Lorenz numbers. In heavily doped n-type silicon (n>1.0×10^{18} cm^{-3}), shallow impurity levels within the band gap start to merge with the conduction band so that the dopants are always completely ionized (Fistul, 1969). With the large band gap of silicon, thermally excited charge carriers contribute negligibly in the investigated temperature range. Therefore, we assume n is fixed at the dopant concentration for all temperatures. The Fermi level E_F in Eq. (25) is calculated according to the n value.

E_d (eV) [a]	m^* (m_0)	v_g (m/s)	Band gap E_g (eV) [b]	d (kg/m^3)	n (cm^{-3})
9.5	1.06	6127	$1.17-4.73\times10^{-4}T^2/(T+636)$	2327	3.93×10^{20}

a Lundstrom, 2000.
b Thourmond, 1975.

Table 1. Parameters used for silicon nanocomposites. Temperature-dependent band gap E_g is used to calculate E_F based on fixed electron concentration n. The electron density of states effective mass is calculated for the lowest conduction band valley. The sound velocity is averaged over TA and LA branches as $v_g=\left\{\left[2v_{g,TA}^{-1}+v_{g,LA}^{-1}\right]/3\right\}^{-1}$.

Despite the variation of grain shapes inside nanocomposites, we can approximate the structure as packed equal-sized cubes. To avoid conflicts between our boundary condition

and grain interface scatterings of phonons, the chosen computational domain boundary must be away from grain interfaces. Here the computational domain is chosen as a cube consisting of eight adjacent cubes, each of which is 1/8 of a cubic grain. In heavily doped polycrystalline silicon, unintentional impurities and imperfections will contribute to impurity scattering and significantly increase the effective A value. Therefore, we cannot predict A based on the doping concentration and A is normally treated as a fitting parameter in analysis. By matching simulation results (empty circles in Fig. 7) with experimental data (filled triangles) at 300 and 573 K, the phonon-impurity scattering coefficient is determined as A=1.0×10^{-43} s^3, which is on the same order as pervious studies for polycrystalline silicon with similar grain sizes (Uma et al., 2001). The divergence between simulation and experimental results is within 6% at both temperatures. Because of the strong internal scatterings of phonons, we find that grain interface scatterings only slightly affect the phonon transport in this nanocomposite. To compare, we use Eq. (26) to calculate the lattice thermal conductivities of bulk silicon with the same internal scatterings of phonons (dashed line in Fig. 7). At 300 and 573 K, adding grain interfaces (open circles) will only reduce the lattice thermal conductivity by less than 6% from its bulk counterpart (dashed line). The weak influence of grain interfaces can be understood from Fig. 8, which shows the accumulative contributions of phonons with different MFPs to the lattice thermal conductivity. Figure 8 indicates that phonons with MFPs longer than 60 nm contribute negligibly to the lattice thermal conductivity at 300 K. At elevated temperatures, internal scatterings of phonons inside grains are significantly enhanced and thus the influence of grain interfaces becomes even weaker. Without conducting time-consuming MC simulations, we can obtain reasonable agreement between our experimental results and calculated lattice thermal conductivities of heavily doped bulk silicon (Fig. 7).

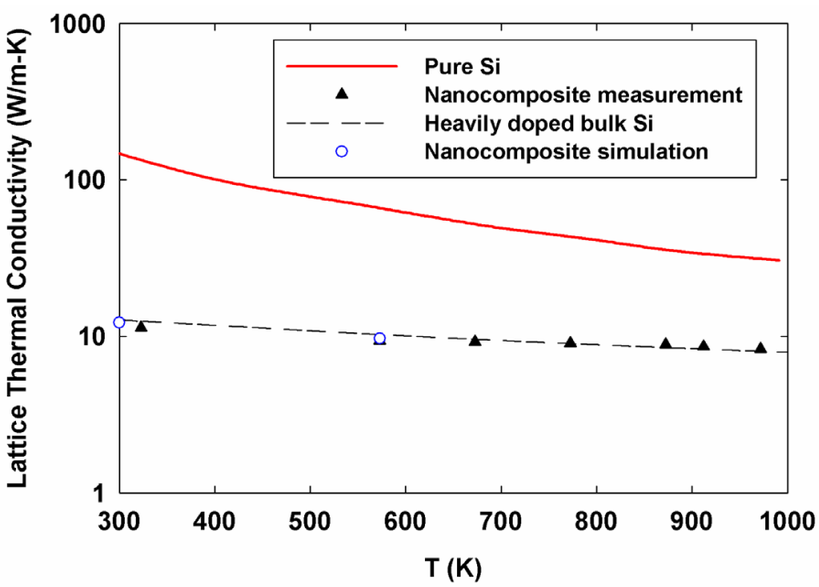

Fig. 7. Lattice thermal conductivities of pure silicon (solid line), measured silicon nanocomposite (filled triangles), calculated heavily doped bulk silicon with electron concentration fixed at n=3.93×10^{20} cm^{-3}, and phonon-impurity scattering coefficient A=1.0×10^{-43} s^3 (dashed line), and simulated 200-nm-grain-size nanocomposite with the same n, A values (empty circles).

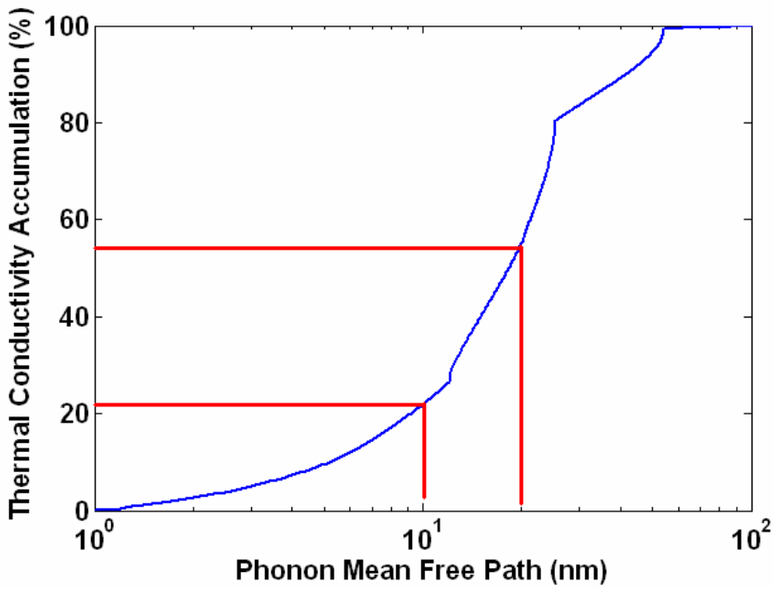

Fig. 8. Room-temperature accumulated thermal conductivity of heavily doped bulk silicon, with electron concentration fixed at n=3.93×10^{20} cm^{-3}, and phonon-impurity scattering coefficient A=1.0×10-43 s^3. The accumulation percentage $a(\Lambda)$ is defined as the percentage of lattice thermal conductivity that is contributed by phonons with MFP less than Λ(Dames & Chen, 2005; Henry & Chen, 2008). From the curve, we can observe that more than 40% of the lattice thermal conductivity is contributed by phonons with MFPs larger than 20 nm, while close to 80% of the lattice thermal conductivity is from phonons with MFPs larger than 10 nm.

To take advantages of the interface scattering of phonons, much smaller grain sizes are required. At 300 K, we find that the room-temperature lattice thermal conductivity can be dropped to 3.0 W/m·K if grain sizes can be reduced to 10 nm, as shown in Fig. 9a. More accurate calculations may further consider the change of A in such small grains with more complicated strain patterns. Due to dominant grain interface scattering, the lattice thermal conductivities for 10 nm grain sizes are insensitive to temperature variations (Fig. 9b). Because Henry and Chen only provided phonon-phonon scattering rates from 300 to 1000 K for our simulations, the lattice thermal conductivity at 1173 K is linearly extrapolated from simulation results for 973 and 773 K. Slight inaccuracy is expected in this treatment due to the weak temperature dependence of lattice thermal conductivities in 10-nm-grain-size samples.

For charge carrier transport inside nanocomposites, we have developed a model based on the BTE under the relaxation-time approximation (Minnich et al., 2009b). The total relaxation time τ for all the scattering mechanisms is obtained by adding up the scattering rates τ_i using Matthiessen's rule $\tau^{-1} = \sum \tau_i^{-1}$ (Lundstrom, 2000; Chen, 2005). Inside a gain, carriers are scattered by acoustic lattice vibrations and ionized impurities (Lundstrom, 2000). On grain interfaces, charge carriers are scattered by a potential barrier created by charges trapped on the interfaces. The grain interface scattering of charge carriers is included into our model by identifying a scattering potential and calculating the corresponding scattering rate, which is then added to the scattering rates of other two mechanisms (Minnich et al., 2009b). Assuming the parameters in Table 1 are unchanged for

10 nm grain sizes, we use the same model to predict k_e and power factors $S^2\sigma$ (Fig. 9c) for two typical grain-interface energy barrier heights U_g (5, 45 meV). The corresponding total thermal conductivities are plotted in Fig. 9b. The power factor and ZT of the reported nano-bulk Si sample (Bux et al., 2009) are also plotted for comparison in Figs. 9c, d. However, its thermal conductivity (not shown in Fig. 9b) cannot be directly compared with the simulated 10-nm-grain-size nanocomposite because this reported sample has a wide distribution of grain sizes (from 10 nm to a few micrometers). In the calculated 10-nm-grain-size nanocomposites, two different barrier heights yield almost identical ZT curves reaching ZT~1.02 at 1173 K (Fig. 9d), which is comparable to conventional SiGe alloys. Figure 9d also shows the predicted ZT of the bulk counterpart, with k_L computed by Eq. (26) (dashed line in Fig. 7) and electrical properties predicted for U_g =0 eV in our electron transport model. Its ZT~0.56 at 1173 K is similar to our measured nanocomposites with 200 nm grain sizes.

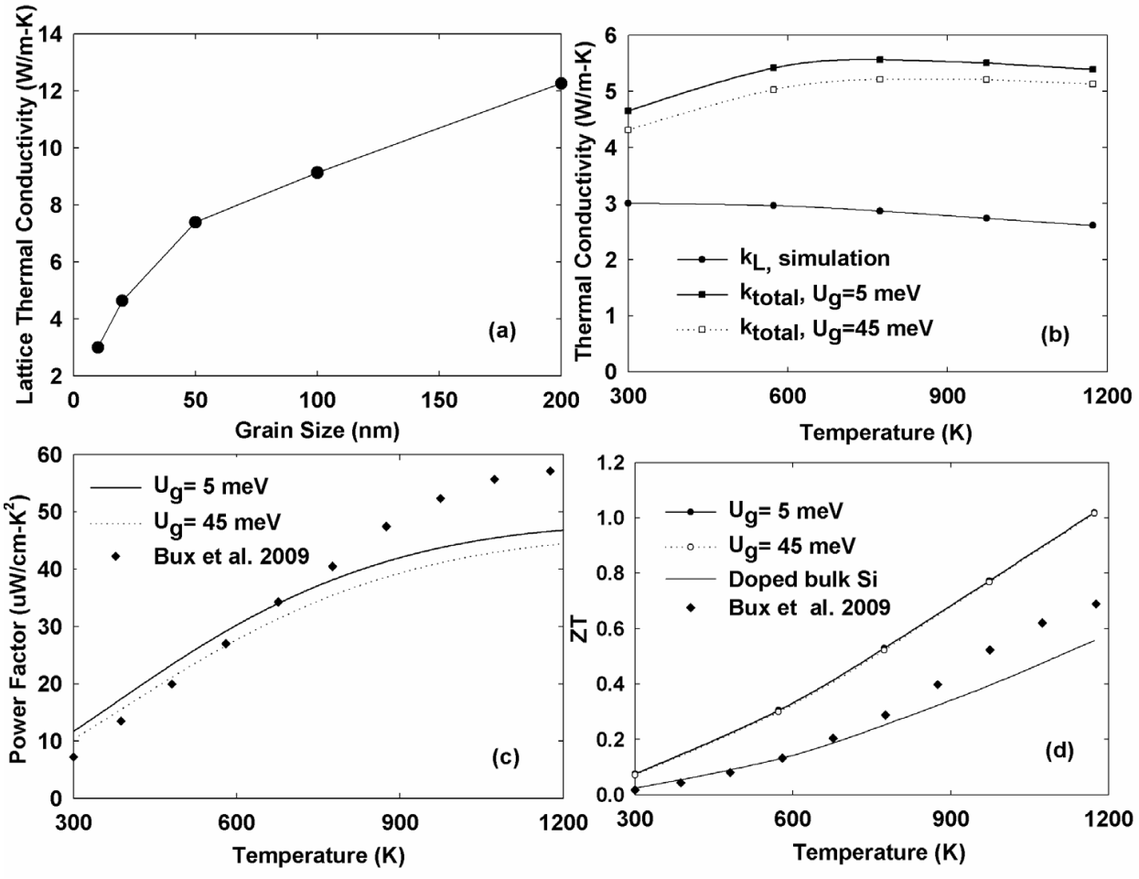

Fig. 9. (a) Grain size dependence of room-temperature k_L for silicon nanocomposites. (b-d) Temperature-dependent properties of the n-type nano-bulk Si sample (Bux et al., 2009) with grain sizes mainly in the 10-100 nm range, and a 10-nm-grain-size silicon nanocomposite with a grain interface barrier height U_g =5, 45 meV: (b) thermal conductivities, (c) power factors, (d) thermoelectric figure of merit, compared to that for the heavily doped bulk counterpart with k_L calculated by Eq. (26) and electrical properties predicted for U_g =0 eV.

Our studies here show that a ZT above 1.0 is achievable in silicon nanocomposites when the grain size is reduced to 10 nm. Compared with SiGe alloys, silicon nanocomposites eliminate the usage of expensive germanium, which makes it more attractive for commercialization. The main challenge here is to effectively prevent the nanograin growth during hot press and conserve the nano-features to scatter phonons (Poudel et al., 2008; Ma et al., 2008; Wang et al., 2008; Joshi et al., 2008; Yang et al., 2009; Zhu et al., 2009; Bux et al., 2009).

6. Summary

In this chapter, frequency-dependent MC simulations are carried out to study the phonon transport inside 2D periodic porous silicon and 3D silicon nanocomposites. A new boundary condition consisting of periodic heat flux with a constant virtual wall temperature is developed for arbitrary periodic structures, enabling accurate thermal conductivity prediction with a single period as the computational domain. This work sets up a framework for future studies of phonon transport in different nanostructures. With accurate information on phonon MFPs in other abundant material systems with good electrical properties, frequency-dependent MC simulations of phonon transport can also be conducted for their corresponding TE nanocomposites. Cheap nanostructured bulk materials with high TE performance can be developed along the way. More broadly, frequency-dependent phonon MC simulations can also provide accurate thermal conductivity predictions for nanostructured materials used in other applications with thermal concerns. Such applications include nanoporous materials for thermal insulation (Chung & Kaviany, 2000), nanoporous electrode materials for batteries (Yamada et al., 2004a; Yamada et al., 2004b; Moriguchi et al., 2006), nanoporous (Logar & Kaučič, 2006) and nanocrystalline (Jurczyk, 2006) hydrogen storage materials.

7. Acknowledgments

This work is supported by “Solid State Solar-Thermal Energy Conversion Center“ (S^3TEC), an Energy Frontier Research Center funded by the U.S. Department of Energy, Office of Science, Office of Basic Energy Sciences under Award Number: DE-SC0001299 (G.C.).

8. References

Alexander, M. N. and Holcomb, D. F. (1968). "Semiconductor-to-Metal Transition in n-Type Group IV Semiconductors." *Reviews of Modern Physics*, Vol. 40(4), pp. 815-829.

Asheghi, M., Kurabayashi, K., Kasnavi, R. and Goodson, K. E. (2002). "Thermal Conduction in Doped Single-Crystal Silicon Films." *Journal of Applied Physics*, Vol. 91(8), pp. 5079-5088.

Broido, D. A., Malorny, M., Birner, G., Mingo, N. and Stewart, D. A. (2007). "Intrinsic Lattice Thermal Conductivity of Semiconductors from First Principles." *Applied Physics Letters*, Vol. 91(23), pp. 231922-3.

Bux, S. K., Blair, R. G., Gogna, P. K., Lee, H., Chen, G., Dresselhaus, M. S., Kaner, R. B. and Fleurial, J.-P. (2009). "Nanostructured Bulk Silicon as an Effective Thermoelectric Material." *Advanced Functional Materials*, Vol. 19(15), pp. 2445-2452.

Cahill, D. G., Ford, W. K., Goodson, K. E., Mahan, G. D., Majumdar, A., Maris, H. J., Merlin, R. and Phillpot, S. R. (2003). "Nanoscale Thermal Transport." *Journal of Applied Physics*, Vol. 93(2), pp. 793-818.

Callaway, J. (1959). "Model for Lattice Thermal Conductivity at Low Temperatures." *Physical Review*, Vol. 113(4), pp. 1046-1051.

Chen, G. (2005). *Nanoscale Energy Transport and Conversion: A Parallel Treatment of Electrons, Molecules, Phonons, and Photons*, Oxford University Press, ISBN-13: 978-0195159424, New York, NY, USA.

Chen, Y., Li, D., Lukes, J. R. and Majumdar, A. (2005). "Monte Carlo Simulation of Silicon Nanowire Thermal Conductivity." *Journal of Heat Transfer*, Vol. 127(10), pp. 1129-1137.

Chung, J. D. and Kaviany, M. (2000). "Effects of Phonon Pore Scattering and Pore Randomness on Effective Conductivity of Porous Silicon." *International Journal of Heat and Mass Transfer*, Vol. 43(4), pp. 521-538.

Dames, C. and Chen, G. (2005). "Thermal Conductivity of Nanostructured Thermoelectric Materials." In: *Thermoelectrics Handbook: Macro to Nano,* Rowe, D. M. (Ed.), pp. 42:1-16, CRC Press, ISBN-13: 978-0849322648, Boca Raton, FL, USA.

Eucken, A. (1932 & 1933). "Thermal Conductivity of Ceramic Refractory Materials: Calculation from Thermal Conductivity of Constituents." *Ceramic Abstracts*, Vol. 11, p. 576, Vol. 12, p. 231.

Fistul, V. I. (1969). *Heavily Doped Semiconductors*, Plenum Press, ISBN-13: 978-0306303524, New York, NY, USA.

Garimella, S. V., Fleischer, A. S., Murthy, J. Y., Keshavarzi, A., Prasher, R., Patel, C., Bhavnani, S. H., Venkatasubramanian, R., Mahajan, R., Joshi, Y., Sammakia, B., Myers, B. A., Chorosinski, L., Baelmans, M., Sathyamurthy, P. and Raad, P. E. (2008). "Thermal Challenges in Next-Generation Electronic Systems." *Components and Packaging Technologies, IEEE Transactions on*, Vol. 31(4), pp. 801-815.

Goldsmid, H. J. (1964). *Thermoelectronic Refrigeration*, Plenum Press, ISBN-13: 978-0306301780, London, UK.

Goodson, K. E., Ju, Y. S. and Asheghi, M. (1997). "Thermal Phenomena in Semiconductor Devices and Interconnects." In: *Microscale Energy Transport*, Tien, C. L., Majumdar, A. and Gerner, F. M. (Eds.), pp. 229-293, Taylor & Francis, ISBN-13: 978-1560324591, Washington, DC.

Hao, Q., Chen, G. and Jeng, M.-S. (2009). "Frequency-Dependent Monte Carlo Simulations of Phonon Transport in Two-Dimensional Porous Silicon with Aligned Pores." *Journal of Applied Physics*, Vol. 106(11), pp. 114321/1-10.

Hao, Q., Zhu, G., Joshi, G., Wang, X., Minnich, A., Ren, Z. and Chen, G. (2010). "Theoretical Studies on the Thermoelectric Figure of Merit of Nano-Grained Bulk Silicon." *Applied Physics Letters*, Vol. 97(6), pp. 063109/1-3.

Henry, A. and Chen, G. (2008). "Spectral Phonon Transport Properties of Silicon Based on Molecular Dynamics Simulations and Lattice Dynamics." *Journal of Computational and Theoretical Nanoscience*, Vol. 5, pp. 141-152.

Hochbaum, A. I., Chen, R., Delgado, R. D., Liang, W., Garnett, E. C., Najarian, M., Majumdar, A. and Yang, P. (2008). "Enhanced Thermoelectric Performance of Rough Silicon Nanowires." *Nature*, Vol. 451(7175), pp. 163-167.

Holland, M. G. (1963). "Analysis of Lattice Thermal Conductivity." *Physical Review*, Vol. 132(6), pp. 2461-2471.

Hsu, K. F., Loo, S., Guo, F., Chen, W., Dyck, J. S., Uher, C., Hogan, T., Polychroniadis, E. K. and Kanatzidis, M. G. (2004). "Cubic $AgPb_mSbTe_{2+m}$: Bulk Thermoelectric Materials with High Figure of Merit." *Science*, Vol. 303(5659), pp. 818-821.

Jeng, M.-S., Yang, R., Song, D. and Chen, G. (2008). "Modeling the Thermal Conductivity and Phonon Transport in Nanoparticle Composites Using Monte Carlo Simulation." *Journal of Heat Transfer*, Vol. 130(4), pp. 042410-11.

Joshi, G., Lee, H., Lan, Y., Wang, X., Zhu, G., Wang, D., Gould, R. W., Cuff, D. C., Tang, M. Y., Dresselhaus, M. S., Chen, G. and Ren, Z. (2008). "Enhanced Thermoelectric Figure-of-Merit in Nanostructured p-Type Silicon Germanium Bulk Alloys." *Nano Letters*, Vol. 8(12), pp. 4670-4674.

Jurczyk, M. (2006). "Nanocrystalline Materials for Hydrogen Storage." *Journal of Optoelectronics and Advanced Materials*, Vol. 8, pp. 418-424.

Kane, E. O. (1957). "Band Structure of Indium Antimonide." *Journal of Physics and Chemistry of Solids*, Vol. 1(4), pp. 249-261.

Klemens, P. G. (1955). "The Scattering of Low-Frequency Lattice Waves by Static Imperfections." *Proceedings of the Physical Society. Section A*, Vol. 68(12), pp. 1113-1128.

Klitsner, T., VanCleve, J. E., Fischer, H. E. and Pohl, R. O. (1988). "Phonon Radiative Heat Transfer and Surface Scattering." *Physical Review B*, Vol. 38(11), pp. 7576-7594.

Kolodziejczak, J. (1961). "Transport of Current Carriers in n-Type Indium Antimonide at Low Temperatures." *Acta Physica Polonica*, Vol. 20, pp. 289-302.

Lacroix, D., Joulain, K. and Lemonnier, D. (2005). "Monte Carlo Transient Phonon Transport in Silicon and Germanium at Nanoscales." *Physical Review B*, Vol. 72(6), pp. 064305/1-11.

Lacroix, D., Joulain, K., Terris, D. and Lemonnier, D. (2006). "Monte Carlo Simulation of Phonon Confinement in Silicon Nanostructures: Application to the Determination of the Thermal Conductivity of Silicon Nanowires." *Applied Physics Letters*, Vol. 89(10), pp. 103104-3.

Lee, J. H., Grossman, J. C., Reed, J. and Galli, G. (2007). "Lattice Thermal Conductivity of Nanoporous Si: Molecular Dynamics Study." *Applied Physics Letters*, Vol. 91(22), pp. 223110-3.

Lindsay, L., and Broido, D.A. (2008). "Three-Phonon Phase Space and Lattice Thermal Conductivity in Semiconductors." *Journal of Physics: Condensed Matter*, Vol. 20, pp. 165209/1-6.

Logar, N. Z. and Kaučič, V. (2006). "Nanoporous Materials: From Catalysis and Hydrogen Storage to Wastewater Treatment." *Acta Chimica Slovenica*, Vol. 53, pp. 117–135.

Lundstrom, M. (2000). *Fundamentals of Carrier Transport*, Oxford University Press, ISBN-13: 978-0521631341, Cambridge, UK.

Ma, Y., Hao, Q., Poudel, B., Lan, Y., Yu, B., Wang, D., Chen, G. and Ren, Z. (2008). "Enhanced Thermoelectric Figure-of-Merit in p-Type Nanostructured Bismuth Antimony Tellurium Alloys Made from Elemental Chunks." *Nano Letters*, Vol. 8(8), pp. 2580-2584.

Maiti, A., Mahan, G. D. and Pantelides, S. T. (1997). "Dynamical Simulations of Nonequilibrium Processes - Heat Flow and the Kapitza Resistance across Grain Boundaries." *Solid State Communications*, Vol. 102(7), pp. 517-521.

Mazumder, S. and Majumdar, A. (2001). "Monte Carlo Study of Phonon Transport in Solid Thin Films Including Dispersion and Polarization." *Journal of Heat Transfer*, Vol. 123(4), pp. 749-759.

McConnell, A. D., and Goodson, K.E. (2005). "Thermal Conduction in Silicon Micro and Nanostructures." *Annual Review of Heat Transfer,* Vol. 14, pp. 129-168.

McGaughey, A. J. H. and Kaviany, M. (2005). "Observation and Description of Phonon Interactions in Molecular Dynamics Simulations." *Physical Review B*, Vol. 71(18), pp. 184305/1-11.

Minnich, A. J., Dresselhaus, M. S., Ren, Z. F. and Chen, G. (2009a). "Bulk Nanostructured Thermoelectric Materials: Current Research and Future Prospects." *Energy & Environmental Science*, Vol. 2(5), pp. 466-479.

Minnich, A. J., Lee, H., Wang, X. W., Joshi, G., Dresselhaus, M. S., Ren, Z. F., Chen, G. and Vashaee, D. (2009b). "Modeling Study of Thermoelectric Sige Nanocomposites." *Physical Review B*, Vol. 80(15), pp. 155327/1-11.

Miyazaki, K., Arashi, T., Makino, D. and Tsukamoto, H. (2006). "Heat Conduction in Microstructured Materials." *Components and Packaging Technologies, IEEE Transactions on*, Vol. 29(2), pp. 247-253.

Moriguchi, I., Hidaka, R., Yamada, H., Kudo, T., Murakami, H. and Nakashima, N. (2006). "A Mesoporous Nanocomposite of TiO_2 and Carbon Nanotubes as a High-Rate Li-Intercalation Electrode Material." *Advanced Materials*, Vol. 18(1), pp. 69-73.

Narumanchi, S. V. J., Murthy, J. Y. and Amon, C. H. (2006). "Boltzmann Transport Equation-Based Thermal Modeling Approaches for Hotspots in Microelectronics." *Heat and Mass Transfer*, Vol. 42(6), pp. 478-491.

Pattamatta, A. and Madnia, C. K. (2009). "Modeling Heat Transfer in Bi_2Te_3-Sb_2Te_3 Nanostructures." *International Journal of Heat and Mass Transfer*, Vol. 52(3-4), pp. 860-869.

Peterson, R. B. (1994). "Direct Simulation of Phonon-Mediated Heat Transfer in a Debye Crystal." *Journal of Heat Transfer*, Vol. 116(4), pp. 815-822.

Poudel, B., Hao, Q., Ma, Y., Lan, Y., Minnich, A., Yu, B., Yan, X., Wang, D., Muto, A., Vashaee, D., Chen, X., Liu, J., Dresselhaus, M. S., Chen, G. and Ren, Z. (2008). "High-Thermoelectric Performance of Nanostructured Bismuth Antimony Telluride Bulk Alloys." *Science*, Vol. 320(5876), pp. 634-638.

Prasher, R. (2006). "Thermal Conductivity of Composites of Aligned Nanoscale and Microscale Wires and Pores." *Journal of Applied Physics*, Vol. 100(3), pp. 034307-9.

Randrianalisoa, J. and Baillis, D. (2008). "Monte Carlo Simulation of Steady-State Microscale Phonon Heat Transport." *Journal of Heat Transfer*, Vol. 130(7), pp. 072404-13.

Song, D. and Chen, G. (2004). "Thermal Conductivity of Periodic Microporous Silicon Films." *Applied Physics Letters*, Vol. 84(5), pp. 687-689.

Swartz, E. T. and Pohl, R. O. (1989). "Thermal Boundary Resistance." *Reviews of Modern Physics*, Vol. 61(3), pp. 605-668.

Tang, J., Wang, H.-T., Lee, D. H., Fardy, M., Huo, Z., Russell, T. P. and Yang, P. (2010). "Holey Silicon as an Efficient Thermoelectric Material." *Nano Letters*, Vol. 10(10), pp. 4279-4283.

Thurmond, C. D. (1975). "The Standard Thermodynamic Functions for the Formation of Electrons and Holes in Ge, Si, Gaas, and Gap." *Journal of The Electrochemical Society*, Vol. 122(8), pp. 1133-1141.

Tian, W. and Yang, R. (2007). "Thermal Conductivity Modeling of Compacted Nanowire Composites." *Journal of Applied Physics*, Vol. 101(5), pp. 054320-5.

Turney, J. E., Landry, E. S., McGaughey, A. J. H. and Amon, C. H. (2009). "Predicting Phonon Properties and Thermal Conductivity from Anharmonic Lattice Dynamics Calculations and Molecular Dynamics Simulations." *Physical Review B*, Vol. 79(6), pp. 064301/1-12.

Uma, S., McConnell, A. D., Asheghi, M., Kurabayashi, K. and Goodson, K. E. (2001). "Temperature Dependent Thermal Conductivity of Undoped Polycrystalline Silicon Layers." *International Journal of Thermophysics*, Vol. 22, pp. 605-616.

Wang, X. W., Lee, H., Lan, Y. C., Zhu, G. H., Joshi, G., Wang, D. Z., Yang, J., Muto, A. J., Tang, M. Y., Klatsky, J., Song, S., Dresselhaus, M. S., Chen, G. and Ren, Z. F. (2008). "Enhanced Thermoelectric Figure of Merit in Nanostructured n-Type Silicon Germanium Bulk Alloy." *Applied Physics Letters*, Vol. 93(19), pp. 193121-3.

Yamada, H., Yamato, T., Moriguchi, I. and Kudo, T. (2004a). "Porous TiO_2 (Anatase) Electrodes for High-Power Batteries." *Chemistry Letters*, Vol. 33(12), pp. 1548-1549.

Yamada, H., Yamatoa, T., Moriguchia, I. and Kudo, T. (2004b). "Interconnected Macroporous TiO_2 (Anatase) as a Lithium Insertion Electrode Material." *Solid State Ionics*, Vol. 175, pp. 195-198.

Yamamoto, A., Takazawa, H. and Ohta, T. (1999). " Thermoelectric Transport Properties of Porous Silicon Nanostructure." *Proceedings of 18th International Conference on Thermoelectrics*, pp. 428-431, ISBN 0-7803-5451-6, Baltimore, MD, USA, Aug 1999 - Sep 1999, IEEE Publications Office, Los Alamitos, CA, USA.

Yamanouchi, C., Mizuguchi, K. and Sasaki, W. (1967). "Electric Conduction in Phosphorus Doped Silicon at Low Temperatures." *Journal of the Physical Society of Japan*, Vol. 22(3), pp. 859-864.

Yang, J., Hao, Q., Wang, H., Lan, Y. C., He, Q. Y., Minnich, A., Wang, D. Z., Harriman, J. A., Varki, V. M., Dresselhaus, M. S., Chen, G. and Ren, Z. F. (2009). "Solubility Study of Yb in n-Type Skutterudites $Yb_xCo_4Sb_{12}$ and Their Enhanced Thermoelectric Properties." *Physical Review B*, Vol. 80(11), pp. 115329.

Yang, R. and Chen, G. (2004). "Thermal Conductivity Modeling of Periodic Two-Dimensional Nanocomposites." *Physical Review B*, Vol. 69(19), pp. 195316/1-10.

Yang, R., Chen, G. and Dresselhaus, M. S. (2005). "Thermal Conductivity of Simple and Tubular Nanowire Composites in the Longitudinal Direction." *Physical Review B*, Vol. 72(12), pp. 125418/1-7.

Yu, J.-K., Mitrovic, S., Tham, D., Varghese, J. and Heath, J. R. (2010). "Reduction of Thermal Conductivity in Phononic Nanomesh Structures." *Nature Nanotechnology*, advance online publication.

Zhu, G. H., Lee, H., Lan, Y. C., Wang, X. W., Joshi, G., Wang, D. Z., Yang, J., Vashaee, D., Guilbert, H., Pillitteri, A., Dresselhaus, M. S., Chen, G. and Ren, Z. F. (2009).

"Increased Phonon Scattering by Nanograins and Point Defects in Nanostructured Silicon with a Low Concentration of Germanium." *Physical Review Letters*, Vol. 102(19), pp. 196803/1-4.

Ziman, J. M. (1956 & 1957). "The Effect of Free Electrons on Lattice Conduction." *Philosophical Magazine*, Vol. 1(2), pp. 191-198, Vol. 2(14), pp. 292.

Applications of Monte Carlo Method in Science and Engineering
Edited by Prof. Shaul Mordechai

ISBN 978-953-307-691-1
Hard cover, 950 pages
Publisher InTech
Published online 28, February, 2011
Published in print edition February, 2011

In this book, Applications of Monte Carlo Method in Science and Engineering, we further expose the broad range of applications of Monte Carlo simulation in the fields of Quantum Physics, Statistical Physics, Reliability, Medical Physics, Polycrystalline Materials, Ising Model, Chemistry, Agriculture, Food Processing, X-ray Imaging, Electron Dynamics in Doped Semiconductors, Metallurgy, Remote Sensing and much more diverse topics. The book chapters included in this volume clearly reflect the current scientific importance of Monte Carlo techniques in various fields of research.

INTECH
open science | open minds

InTech Europe
University Campus STeP Ri
Slavka Krautzeka 83/A
51000 Rijeka, Croatia
Phone: +385 (51) 770 447
Fax: +385 (51) 686 166
www.intechopen.com

InTech China
Unit 405, Office Block, Hotel Equatorial Shanghai
No.65, Yan An Road (West), Shanghai, 200040, China
中国上海市延安西路65号上海国际贵都大饭店办公楼405单元
Phone: +86-21-62489820
Fax: +86-21-62489821

IntechOpen